Bianisotropic Acoustic Metasurface for Surface-Wave-Enhanced Wavefront **Transformation**

Junfei Lio, 1,* Ailing Songo, 1,2 and Steven A. Cummer^{1,†}

¹Department of Electrical and Computer Engineering, Duke University, Durham, North Carolina 27708, USA ²School of Mechanical Engineering, Xi'an Jiaotong University, Xi'an, Shaanxi 710049, China

(Received 26 May 2020; revised 20 August 2020; accepted 25 August 2020; published 8 October 2020)

Recent advances in metasurfaces have shown that efficient wavefront transformation can be obtained by carefully designing the bianisotropic response of the metasurfaces. However, as will be shown in this paper, applying such a scheme for complicated wavefront transformations will lead to nonreciprocal local response, which is difficult to realize physically, if the field is not designed properly. In this paper, we identify the local power conservation requirement and introduce surface waves into the scattered field to meet such requirements. Based on such a scheme, we develop a bianisotropic metasurface design approach for near-perfect arbitrary beam splitting and anomalous reflection. Such a passive and reciprocal design approach enables experimental demonstration of surface-wave-enhanced wavefront transformation.

DOI: 10.1103/PhysRevApplied.14.044012

I. INTRODUCTION

The ability to fully control the behavior of acoustic waves has long been desired and is at present a highly active research area. In this regard, metamaterials and metasurfaces have served as a primary approach in recent years [1-3]. Metasurfaces mold the wave propagation within a thin planar or nearly flat geometry by packing phase shifts along the gradient metasurface. Many innovative low-profile devices that manipulate the transverse phase profile have been reported [4,5], showing the immense potential of these surfaces in physics and engineering.

While the early metasurfaces for wavefront engineering attracted considerable attention, it was soon found that these metasurfaces suffer from limited power efficiency. The efficiency of phase-shift devices is fundamentally restricted by reflection and scattering into unwanted directions or modes. To achieve a high (or controlled) transmission magnitude into a mode with an arbitrary transmission phase, many unit cell designs have been proposed [4,6–11]. Nevertheless, it was recently recognized that, for both reflection-type and transmission-type metasurfaces, a phase-constraint design scheme does not provide full control over the scattered waves [12–17]. Therefore, the power efficiency for these metasurfaces is limited.

For reflection-type metasurfaces, rigorous analysis shows that efficiency limits come from the interference between the incident and the reflected fields, which causes intensity and power modulation along a planar surface [13]. Such power flow redistribution could be realized with controlled loss and gain within the unit cells, but this is difficult to achieve in practice. For the passive realization of a theoretically perfect wavefront transformation, several approaches have been proposed. For example, the power redistribution along the metasurface can be fulfilled by engineering surface waves in electromagnetics [18], or controlling the nonlocal effects in both electromagnetics [15] and acoustics [19]. Another approach is to control the shape of the metasurface so that the power does not enter or emerge from the metasurface [20].

For ideal transmission-type metasurfaces, the phase profile modulation must be accompanied by a suitable change in the field amplitudes, due to the inevitable variation of the wave impedance [16,17]. Thus, designing unit cells with uniform (unity) transmission amplitude and arbitrary phase will not necessarily yield efficient wavefront transformation. Recent advances have demonstrated that, for electromagnetic waves, precise control over the phase and suitable wave impedance matching can be achieved simultaneously by carefully controlling the bianisotropy of the unit cells [12,18,21]. Acoustic bianisotropy, also known as Willis coupling [22-24], has been extended to acoustic metasurfaces to overcome the power limits for phase-modulation metasurfaces [16,17,25]. By defining the desired fields on both sides of the metasurface and calculating the required impedance matrix, beam steering devices with near-unity power efficiency have been designed [16,17].

Then a question naturally arises: can the bianisotropic wave impedance approach be applied for more

^{*}junfei.li@duke.ed

[†]cummer@ee.duke.edu

complicated wavefront transformation applications? This question seems trivial at first glance. However, as has been demonstrated for the electromagnetic scenario [18,26], when the incident and transmitted waves are not single plane waves, interference between multiple modes will locally modulate the power flow, causing a power flow mismatch across the unit cells, which prevents simple implementation using passive structures. Potential lossless solutions have been proposed in Ref. [14]; nonetheless, it was implied that these would require nonreciprocal or nonlocal elements, whose passive implementation prospects are unclear. For electromagnetic waves, the idea of using self-excited surface waves to redirect the power flow has been proposed to balance the local power flow on both sides of the metasurface [18]. However, it only deals with equal beam splitting, and no experimental demonstration has been reported so far. To date, the discussion of realizing structured surfaces with near-unity power efficiency has been scarce in acoustics [16,17,19,20,25,27], and how to design high-efficiency acoustic metasurfaces that involve complicated functionalities remain elusive.

In this paper, we introduce self-induced surface waves into acoustic metasurfaces as a means to meet the local power conservation requirement and develop an approach for designing bianisotropic metasurfaces for arbitrary beam splitting and anomalous reflection with theoretically 100% power efficiency. The design strategy is examined with four cases: equal splitting, wave splitting into two different directions with specified intensity ratio, anomalous reflection, and simultaneous control over the reflection and transmission. The design is verified with both simulations and experiments.

Conventionally, designing highly efficient acoustic metasurfaces for transmission requires designing unit cells with high transmission amplitudes; while for reflection-type metasurfaces, hard boundaries are preferred. However, our study shows an interesting and counterintuitive finding: when we design transmission-type metasurfaces, higher efficiency can be achieved by allowing controlled reflected fields; while for reflection-type metasurfaces, allowing a nonzero transmitted field can be the key to achieving ideal reflection.

II. TRANSMISSION CASE: ARBITRARY BEAM SPLITTING

A. Origin of the power efficiency limit

We first investigate a transmission-type metasurface that splits a normally incident wave into two plane waves with transmitted angles θ_1 , θ_2 and transmission coefficients $T_{1,2} = t_{1,2}e^{j\phi_{1,2}}$. Here we impose $\phi_1 = \phi_2$ for simplicity. (Since the waves are propagating in different directions, we can always find a position where $\phi_1 = \phi_2$ is satisfied, and set that point as the origin.) The normally incident wave is

written as

$$p_1 = p_0 e^{-jky}, (1)$$

$$v_{1,y} = \frac{p_0}{Z_0} e^{-jky}. (2)$$

The desired transmitted fields are

$$p_2 = T_1 p_0 e^{jk \sin \theta_1 x} e^{-jk \cos \theta_1 y} + T_2 p_0 e^{-jk \sin \theta_2 x} e^{-jk \cos \theta_2 y},$$
(3)

$$v_{2,y} = \frac{T_1 p_0 \cos \theta_1}{Z_0} e^{jk \sin \theta_1 x} e^{-jk \cos \theta_1 y} + \frac{T_2 p_0 \cos \theta_2}{Z_0} e^{-jk \sin \theta_2 x} e^{-jk \cos \theta_2 y}.$$
 (4)

The global power flow perpendicular to the metasurface needs to be conserved, i.e.,

$$\frac{t_1^2|p_0|^2\cos\theta_1}{2Z_0} + \frac{t_2^2|p_0|^2\cos\theta_2}{2Z_0} = \frac{|p_0|^2}{2Z_0};$$
 (5)

thus,

$$t_1^2 \cos \theta_1 + t_2^2 \cos \theta_2 = 1. \tag{6}$$

On the transmission side, the pressure and normal velocity fields at the metasurface (y = 0) are

$$p_{20} = T_1 p_0 e^{jk \sin \theta_1 x} + T_2 p_0 e^{-jk \sin \theta_2 x},$$
 (7)

$$v_{2,y0} = \frac{T_1 p_0 \cos \theta_1}{Z_0} e^{jk \sin \theta_1 x} + \frac{T_2 p_0 \cos \theta_2}{Z_0} e^{-jk \sin \theta_2 x}.$$
 (8)

The impedance matrix profile of a metasurface can be calculated by putting the defined fields on both sides of the metasurface into the impedance matrix definition

$$\begin{bmatrix} p_1(x,0) \\ p_2(x,0) \end{bmatrix} = \begin{bmatrix} Z_{11} & Z_{12} \\ Z_{21} & Z_{22} \end{bmatrix} \begin{bmatrix} \mathbf{n} \cdot \mathbf{v_1}(x,0) \\ -\mathbf{n} \cdot \mathbf{v_2}(x,0) \end{bmatrix}, \tag{9}$$

and equating the real and imaginary parts, respectively. Note that, for passive and lossless structures, all the components in the impedance matrix shall be purely imaginary [16,17].

As an illustration, we calculated the impedance matrix in the equal splitting case, where $\theta_1 = \theta_2 = 60^\circ$, $t_1 = t_2 = 1/\sqrt{2\cos\theta_{1,2}}$, $\phi_1 = \phi_2 = \pi/2$, and the imaginary part of the impedance matrix is plotted in Fig. 1(a). Here X = Im[Z], denoting the reactance. From Fig. 1(a), we can see that $Z_{12} \neq Z_{21}$. This result implies that a metasurface that performs such a wavefront transformation must

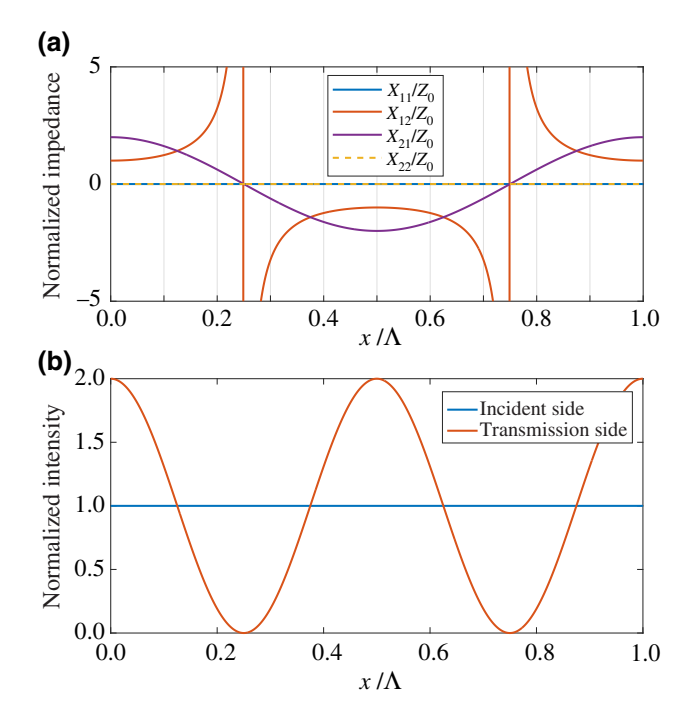


FIG. 1. Impedance requirement (imaginary part) and power distribution for an ideal beam splitting metasurface. (a) Required impedance matrix profile along the metasurface, normalized by Z_0 . Here $Z_{12} \neq Z_{21}$ implies nonreciprocity within the unit cells. (b) Intensity profile on both sides of the metasurface, normalized by the incident sound intensity. Such a power flow mismatch on both sides requires energy exchange within the metasurface.

be nonreciprocal. This is extremely difficult to physically implement in a passive acoustic system.

For further insight, we examine the intensity field $I = \frac{1}{2} \text{Re}[p v^*]$. The transmitted intensity field along the metasurface is given by

$$I_{2,y0} = \frac{|p_0|^2}{2Z_0} \{ 1 + t_1 t_2 (\cos \theta_1 + \cos \theta_2) \times \cos [k(\sin \theta_1 + \sin \theta_2)x] \}.$$
 (10)

From Eq. (10) we can see that the interference between two transmitted beams makes the transmitted intensity along the metasurface nonuniform, as shown in Fig. 1(b). However, the incident plane wave creates a uniform intensity profile on the incident side. Such a power flow mismatch shares many similarities with the reflection case [13], meaning that the metasurface needs to either embed gain and loss to absorb the energy in some regions and emit energy in others or provide mechanisms, such as nonlocality, to transport power transversely across the metasurface.

B. Power balancing with surface waves

As discussed in the previous section, the difficulty of a theoretically perfect wavefront transformation with

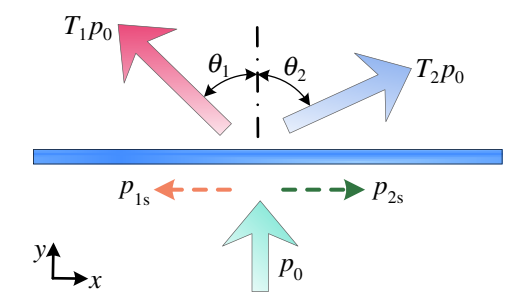


FIG. 2. Illustration of the beam splitting scenario under study. A normally incident wave is ideally split into two waves with transmitted angles θ_1 and θ_2 by creating auxiliary surface waves on the incident side.

transmission-type metasurfaces lies in that we need a proper mechanism to carry the energy among different regions of the metasurface. Such a requirement can also be met by carefully designing surface waves into the scattered field to carry the energy along the surface. In order to match the intensity profile on both sides of the metasurface, two counterpropagating surface waves are introduced on the incident side, as illustrated in Fig. 2. Note that the surface waves can be added on either side of the metasurface and that here the incident side is chosen for simplicity. The total pressure field on the incident side is now

$$p_1 = p_0 e^{-jky} + p_{1s} e^{\alpha_1 y} e^{jk_1 x} + p_{2s} e^{\alpha_2 y} e^{-jk_2 x}, \tag{11}$$

where $k_1 = \sqrt{k^2 + \alpha_1^2}$, $k_2 = \sqrt{k^2 + \alpha_2^2}$, $p_{1s} = a_1 e^{j\beta_1} p_0$ and $p_{2s} = a_2 e^{j\beta_2} p_0$ are the complex amplitudes for both surface waves, and α_1 and α_2 are their respective decay rates. Then

$$p_1 = p_0 e^{-jky} + a_1 p_0 e^{\alpha_1 y} e^{j(k_1 x + \beta_1)} + a_2 p_0 e^{\alpha_2 y} e^{j(-k_2 x + \beta_2)}.$$
(12)

The normal velocity field is

$$v_{1,y} = \frac{p_0}{Z_0} e^{-jky} + \frac{ja_1\alpha_1 p_0}{kZ_0} e^{\alpha_1 y} e^{j(k_1 x + \beta_1)} + \frac{ja_2\alpha_2 p_0}{kZ_0} e^{\alpha_2 y} e^{j(-k_2 x + \beta_2)}.$$
 (13)

At the position of the metasurface (y = 0), the pressure and normal velocity fields on the incident side are

$$p_{10} = p_0 + a_1 p_0 e^{j(k_1 x + \beta_1)} + a_2 p_0 e^{j(-k_2 x + \beta_2)}, \qquad (14)$$

$$v_{1,y_0} = \frac{p_0}{Z_0} + \frac{ja_1\alpha_1p_0}{kZ_0}e^{j(k_1x+\beta_1)} + \frac{ja_2\alpha_2p_0}{kZ_0}e^{j(-k_2x+\beta_2)}.$$
(15)

The incident intensity field $[I_y = \frac{1}{2} \text{Re}(p v_y^*)]$ is calculated as

$$I_{1,y0} = \frac{|p_0|^2}{2Z_0} \left[1 + a_1 \cos(k_1 x + \beta_1) - \frac{a_1 \alpha_1}{k} \sin(k_1 x + \beta_1) + a_2 \cos(k_2 x - \beta_2) + \frac{a_2 \alpha_2}{k} \sin(k_2 x - \beta_2) - \frac{a_1 a_2 (\alpha_1 - \alpha_2)}{k} \sin(k_1 x + \beta_1 + k_2 x - \beta_2) \right].$$
(16)

To realize the local power conservation condition, $I_{2,y0}$ and $I_{1,y0}$ should be equal. This equation has many solutions, but by setting $\beta_1 = \beta_2 = 0$, $a_1 = a_2 = a$, and $\alpha_1 = \alpha_2 = \alpha$ we can immediately find one of them. In this case, $I_{1,y0}$ becomes

$$I_{1,y0} = \frac{|p_0|^2}{2Z_0} [1 + 2a\cos(\sqrt{k^2 + \alpha^2}x)].$$
 (17)

Comparing Eqs. (10) and (17), we can see that several conditions must be met for $I_{1,y0} = I_{2,y0}$ that define the amplitude and wave number of the surface waves, namely,

$$a = \frac{t_1 t_2 (\cos \theta_1 + \cos \theta_2)}{2},\tag{18}$$

$$\alpha = k\sqrt{(\sin\theta_1 + \sin\theta_2)^2 - 1}.\tag{19}$$

Note that there are lots of combinations of surface waves on both sides that could do the same job, and the solution provided here is not unique. Once the field satisfies the local power conservation requirement, the impedance profile can be achieved with passive lossless bianisotropic metasurface designs. The impedance matrix profile can thus be calculated by putting the total fields, including the two additional surface waves, into Eq. (9).

C. Verification with simulation using the three-layer approach

In the first demonstration, we examine an equal-splitting case where the transmitted angle is $\theta_1 = \theta_2 = 60^\circ$, $t_1 = t_2 = 1/\sqrt{2\cos\theta_{1,2}} = 1$, $\phi_1 = \phi_2 = \pi/2$, and the incident pressure $p_0 = 1$ Pa. In this case, a = 0.5, $\alpha = \sqrt{2}k$. With the pressure and normal velocity fields on both sides of the metasurface, the impedance matrix profile within a period can be calculated; see Fig. 3(a). We can see that, with balanced local power, $Z_{12} = Z_{21}$ confirms the reciprocity of the unit cells. Here $Z_{11} \neq Z_{22}$ indicates that bianisotropic unit cells are needed. For realization in the simulation, we chose the three-layer model proposed in Ref. [16]. The distance between adjacent layers is set as 5 mm.

The scattered fields from the theoretical calculation and COMSOL simulation are plotted in Figs. 3(b) and 3(c), respectively. In our case, the metasurface is discretized into ten unit cells per period. From the figures, we can see excellent agreement between the theoretical calculation and simulation. Again, there is no unwanted scattering, and all the incident power is directed to the output field,

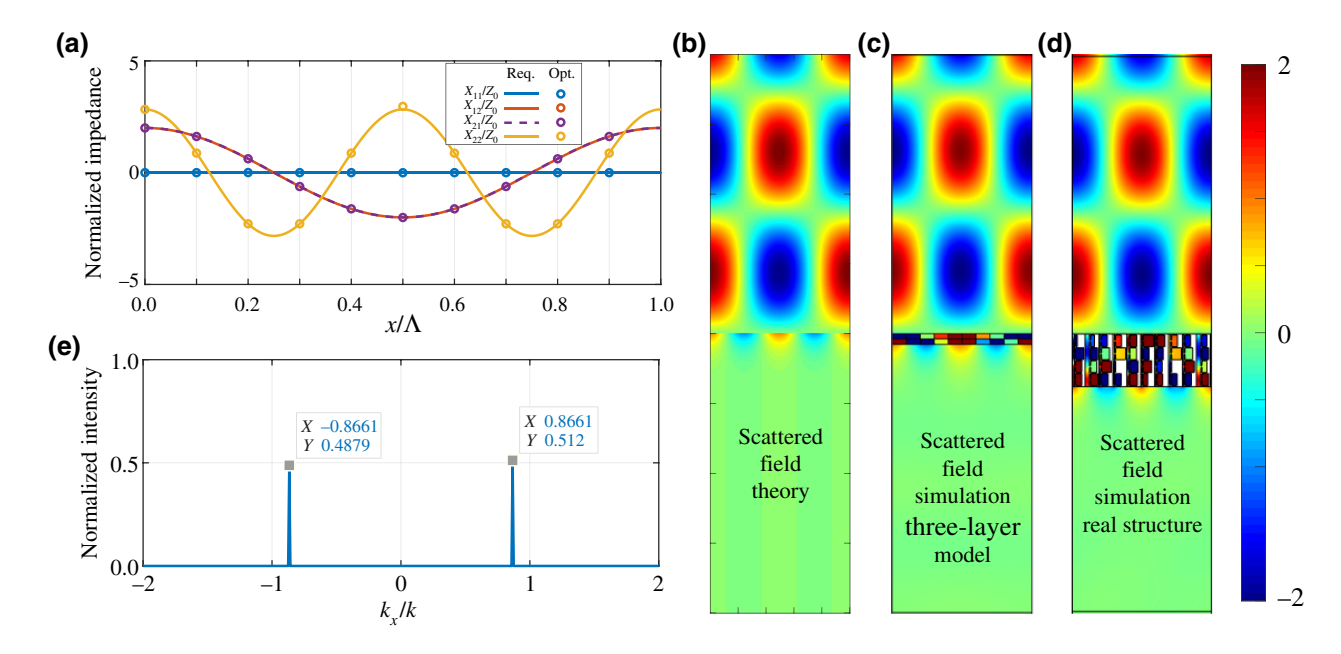


FIG. 3. Design and performance of the beam splitter for equal splitting. (a) Comparison between the impedance matrix requirement along the metasurface and realized values from optimization. (b) Theoretically calculated scattered field. (c) Scattered field with the three-layer model. (d) Scattered field with real structure. (e) Mode analysis of the output field.

showing the effectiveness of the proposed metasurface design.

D. Structure design and verification with simulation and experiment

To realize the desired impedance matrix profile in experiments, we adopted the four-resonator structure described in Ref. [17]; see Fig. 9 in Appendix A for a schematic view. The parameters of the input field and the desired field are kept the same as described in the previous section. In this case, the periodicity is $\Lambda = 132$ mm. For realization, the metasurface is discretized into ten unit cells per period, so the width of each unit cell is w = 13.2 mm. The wall thickness is t = 1 mm, the neck width is s = 1.5mm, and the cavity width is l = 11.25 mm. The impedance matrix is controlled by tuning the channel width w_1 , and the height of each cavity w_a , w_b , w_c , and w_d . The values of these parameters are determined with two steps. They are first optimized using the genetic algorithm (GA). The impedance matrix in the GA optimization is analytically calculated and the cost function is defined as

$$cost = \sqrt{\sum_{i,j=1,2} |Z_{ij}^s - Z_{ij}^t|^2},$$
 (20)

where superscripts "s" and "t" stand for the impedance matrix of the four-resonator structure and theoretical requirement, respectively.

In the second step, the parameters obtained from the GA are set as the initial values, and are further optimized locally using the pattern search (PS) algorithm. During the PS optimization, the impedance matrix of a given structure is retrieved with COMSOL simulations. The first step uses analytically calculated values because its computational speed allows a fast and vast amount of random search within a large space, while in the second step, we retrieve the impedance from simulations to guarantee the calculation accuracy. The optimized geometric parameters are given in Table I (Appendix A).

A comparison between the required impedance matrix profile within a period of the metasurface and the discretized impedance matrices achieved by structure optimization is given in Fig. 3(a). The required impedance profile is closely fulfilled by the optimized structures. The corresponding scattered field with real structure simulation is plotted in Fig. 3(d). Excellent agreement can be found between the real structure design, the three-membrane model, and the theoretical fields. To quantify its power efficiency, we calculate the integral of the normal intensity on the transmission side and compare the value with the incident intensity. In the simulation, the total transmitted power efficiency reaches 99.94% and only 0.06% of the incident power is reflected. Then we take the complex pressure field along the metasurface on the transmission

side and perform a Fourier transform to calculate its farfield radiation pattern. The power scattered into each mode (normal intensity) associated with a certain wave number k_x is calculated with

$$I_n(k_x) = \frac{|p(k_x)|^2 \sqrt{1 - (k_x/k)^2}}{\sum_{-k}^k |p(k_x)|^2 \sqrt{1 - (k_x/k)^2}},$$
 (21)

and the result is shown in Fig. 3(e). On the total transmission side, the power coupled into two desired directions $(k_x/k = \pm \sqrt{3}/2)$, 51.20% and 48.79%. The slight deviation from an ideal field can be attributed to the finite discretization and the tolerated error in the optimization algorithms.

The sample is then fabricated and tested in a twodimensional waveguide. The sample is fabricated with stereolithography 3D printing. The fabricated sample and experimental setup are shown in Fig. 4(a). In the experiment, the speaker array sends a pulse, which is Gaussian modulated in both space and time, normally to the metasurface. The signal is recorded by a moving microphone, and the field is mapped by scanning the region of interest. The steady-state field is mapped by performing the Fourier transform to the time-gated signal at each position and taking the frequency component of interest.

The simulation and the corresponding experimentally measured fields are shown in Figs. 4(b) and 4(c). The fields in the experiment showed good agreement with simulations. In the experiment, the surface wave decaying away from the metasurface can be observed. The far-field radiation is calculated by analyzing the fields along the transmission side of the metasurface. In the experiment, the peak of the output radiation reaches its maximum at -59° and 58° . The ratio of the amplitudes between the two transmitted waves is 0.9256, closely following the design value of 1. Several sources for the small discrepancy are the fabrication error, the loss in the air, sound speed change due to the temperature, and humidity variation in the environment.

E. Arbitrary beam splitting metasurface design

We now investigate a metasurface that splits the incident wave into two different splitting angles and an arbitrary power ratio. As an example, two transmitted angles are chosen as $\theta_1 = 36.87^\circ$, $\theta_2 = 64.16^\circ$, $\phi_1 = \phi_2 = 3\pi/4$, so the periodicity of the metasurface is $\Lambda = 2\pi/(3k/10) = 381.1$ mm. The reason for choosing these two angles is to make the periodicity not infinite, so the realization is simpler. According to the global power conservation condition $t_1^2 \cos \theta_1 + t_2^2 \cos \theta_2 = 1$, we can realize any power distribution between two transmitted waves. In this case, we assume that $t_1^2/t_1^2 = 2$; then the amplitude of the transmission coefficients are $t_1 = 0.99$ and $t_2 = 0.70$, which means that the metasurface can theoretically send 78.59% and

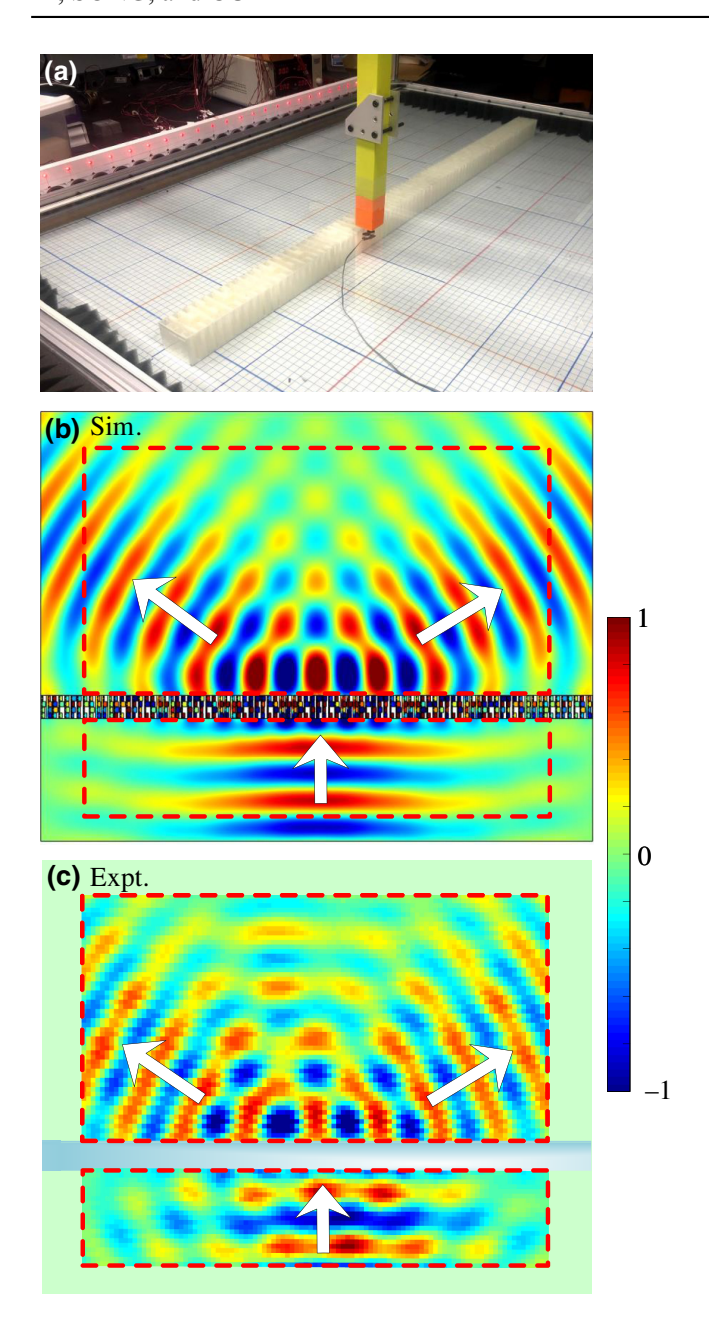


FIG. 4. (a) Sample and experimental setup. (b) Simulated field illuminated by a Gaussian beam. (c) Measured field illuminated by a Gaussian beam.

21.41% of the incident power in the θ_1 and θ_2 directions, respectively. From the above theoretical analysis, a = 0.43 and $\alpha = 1.118k$ in this design.

With the pressure and normal velocity field on both sides of the metasurface, the impedance matrix profile within a period can be calculated; see Fig. 5(a). We see that $Z_{12} = Z_{21}$ with the balanced local power, which confirms the reciprocity of the unit cells. Also, bianisotropic unit cells are needed because $Z_{11} \neq Z_{22}$. For physical realization, the metasurface is discretized into 30 unit cells per period, so the width of each unit cell is w = 12.7 mm. Here

a uniform displacement is added to the entire metasurface to avoid extreme values in the impedance matrix. The scattered fields in theory and in simulation with the three-layer model are plotted in Figs. 5(b) and 5(c), respectively. We see excellent agreement between the theoretical calculation and numerical simulation, and no unwanted scattering occurs in the incident region.

The four-resonator structure is also adopted to realize the desired impedance matrix profile. The impedance matrix is controlled by tuning the channel width w_1 , and the height of each cavity w_a , w_b , w_c , and w_d . These parameters are determined with the GA optimization and PS optimization, and the optimized geometric parameters are given in Table II (Appendix A). In Fig. 5(a) we show the required impedance matrix profile and the discretized impedance matrices achieved by structure optimization, which indicates that the required impedance profile is closely fulfilled by the optimized structures. The scattered field with real structure simulation is shown in Fig. 5(d). We find excellent agreement between the real structure design, the three-membrane model, and the theoretical fields. The slight reflection in the simulation with real structure can be attributed to the finite discretization and the tolerated error in the optimization algorithms. We then performed a Fourier transform of the complex pressure field along the metasurface on the transmission side and calculated the power scattered into each mode associated with a certain k_x ; the result is shown in Fig. 5(e). On the transmission side, the power coupled into two desired directions, 76.74% and 21.29%. The total transmitted power efficiency reaches 98.03%, only 1.97% of the incident power is scattered into unwanted modes.

III. REFLECTION CASE: REDIRECTING THE SOUND

A. Designing the field with balanced power

In this case, we aim at fully coupling a plane wave with incident angle θ_i to a plane wave reflected towards θ_r with 100% power efficiency, as illustrated in Fig. 6. Denote the reflection coefficient by $R = re^{j\phi}$. The pressure field below the metasurface can thus be written as

$$p_1 = p_0 e^{-jk\sin\theta_i x} e^{-jk\cos\theta_i y} + Rp_0 e^{-jk\sin\theta_r x} e^{jk\cos\theta_r y}.$$
 (22)

The normal power conservation requires $r = \sqrt{\cos \theta_i / \cos \theta_r}$. The pressure and normal velocity fields at the position of the metasurface (y = 0) are

$$p_1 = p_0 e^{-jk \sin \theta_i x} + r e^{i\phi} p_0 e^{-jk \sin \theta_r x},$$
 (23)

$$v_{1,y} = \frac{p_0 \cos \theta_i}{Z_0} e^{-jk \sin \theta_i x} - r e^{j\phi} \frac{p_0 \cos \theta_r}{Z_0} e^{-jk \sin \theta_r x}. \quad (24)$$

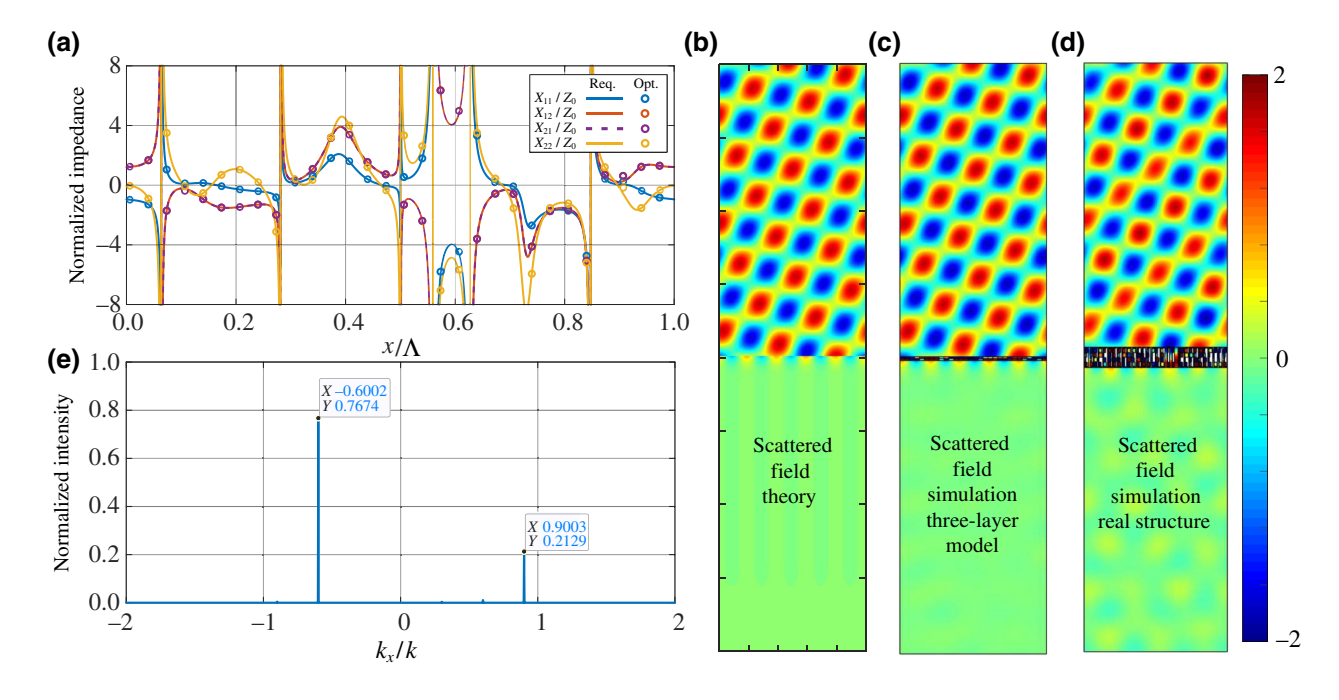


FIG. 5. Design and performance of the beam splitter with different splitting angles and an arbitrary power flow ratio. (a) Comparison between the impedance matrix requirement along the metasurface and realized values from optimization. (b) Theoretically calculated scattered field. (c) Scattered field with the three-layer model. (d) Scattered field with real structure. (e) Mode analysis of the output field.

The intensity field $[I_y = \frac{1}{2} \text{Re}(pv_y^*)]$ along the metasurface is calculated as

$$I_{1,y} = \frac{|p_0|^2 r(\cos\theta_i - \cos\theta_r)}{2Z_0} \cos[k(\sin\theta_i - \sin\theta_r)x + \phi]. \tag{25}$$

We can see that this intensity profile requires an exchange of energy across regions of the metasurface. Now we introduce two auxiliary surface-wave fields on the transmission side of the metasurface. The interference of these two surface waves can provide the mechanism of energy redistribution, but they do not radiate into the far field, enabling ideal power conversion of the incident wave to the desired reflected wave. The total pressure field on the transmission side is defined as

$$p_2 = p_{1s}e^{-\alpha_1 y}e^{-jk_1 x} + p_{2s}e^{-\alpha_2 y}e^{-jk_2 x},$$
 (26)

where $k_1=\sqrt{k^2+\alpha_1^2},\ k_2=\sqrt{k^2+\alpha_2^2},\ p_{1s}=a_1e^{j\,\beta_1}p_0,$ and $p_{2s}=a_2e^{j\,\beta_2}p_0.$ Thus,

$$p_2 = a_1 p_0 e^{-\alpha_1 y} e^{j(\beta_1 - k_1 x)} + a_2 p_0 e^{-\alpha_2 y} e^{j(\beta_2 - k_2 x)}.$$
 (27)

The normal velocity field is

$$v_{2,y} = -\frac{ja_1\alpha_1p_0}{kZ_0}e^{-\alpha_1y}e^{j(\beta_1 - k_1x)} - \frac{ja_2\alpha_2p_0}{kZ_0}e^{-\alpha_2y}e^{j(\beta_2 - k_2x)}.$$
(28)

The pressure and normal velocity fields at the metasurface (y = 0) are thus

$$p_{20} = a_1 p_0 e^{j(\beta_1 - k_1 x)} + a_2 p_0 e^{j(\beta_2 - k_2 x)},$$
 (29)

$$v_{2,y0} = -\frac{ja_1\alpha_1p_0}{kZ_0}e^{j(\beta_1 - k_1x)} - \frac{ja_2\alpha_2p_0}{kZ_0}e^{j(\beta_2 - k_2x)}.$$
 (30)

The normal intensity field is

$$I_{2,y} = \frac{|p_0|^2 a_1 a_2 (\alpha_2 - \alpha_1)}{2kZ_0} \cos\left[(k_1 - k_2)x + \beta_2 - \beta_1 + \frac{\pi}{2} \right].$$
(31)

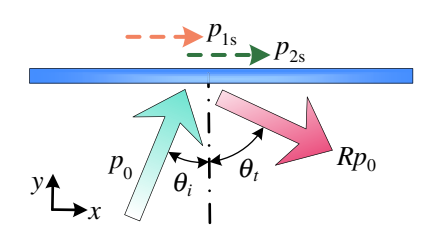


FIG. 6. Illustration of the reflective metasurface under study. A plane incident wave is ideally reflected to an angle θ_r by creating surface waves on the transmission side.

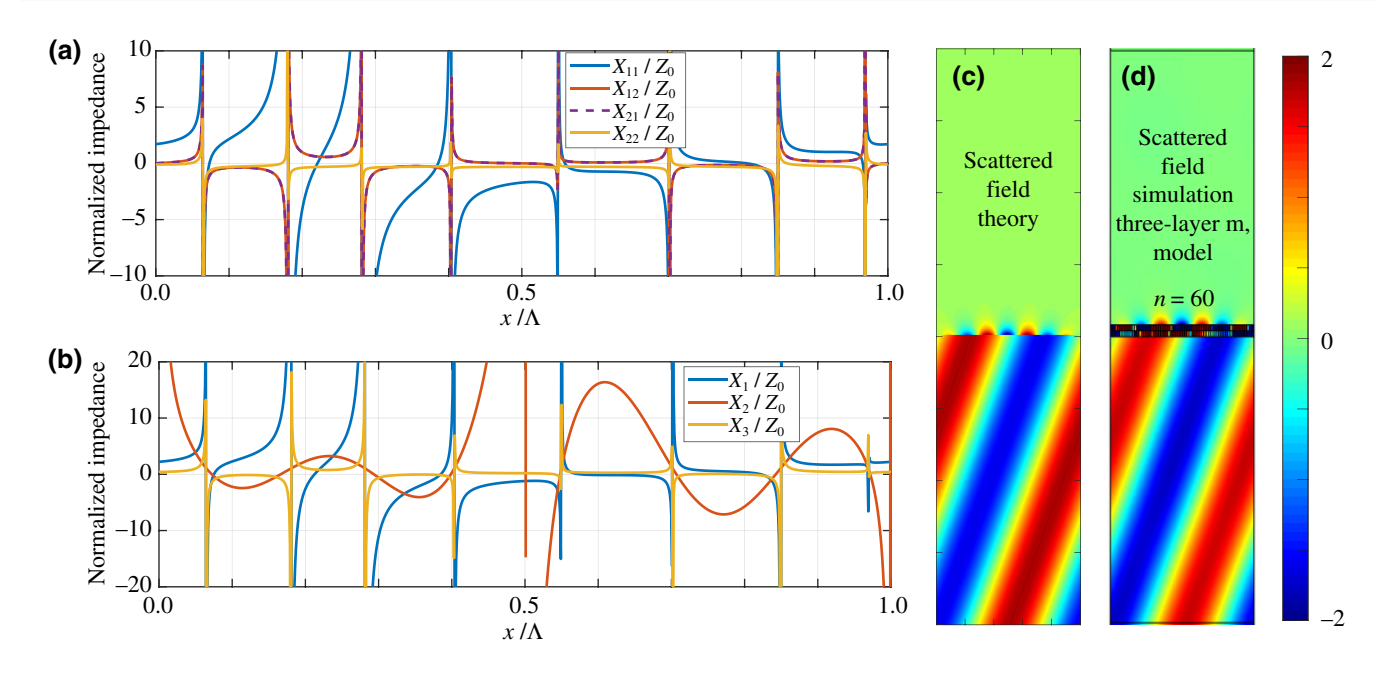


FIG. 7. Design and performance of the reflective metasurface. (a) The imaginary part of the impedance matrix along the metasurface within a period. (b) The imaginary part of the impedances for the three layers. (c) Theoretically calculated scattered field. (d) The scattered field in the simulation, showing good agreement with the theory.

Comparing Eq. (31) with Eq. (25), we see that, in order for them to be matched, we need

$$\beta_2 - \beta_1 + \frac{\pi}{2} = \phi, \tag{32}$$

$$k_1 - k_2 = k(\sin \theta_i - \sin \theta_r), \tag{33}$$

$$a_1 a_2 = \frac{kr(\cos \theta_i - \cos \theta_r)}{\alpha_2 - \alpha_1},\tag{34}$$

where a_1 , β_1 , k_1 , and ϕ can be arbitrary.

Once the local power conservation condition is met, we can design the bianisotropic metasurface with purely passive structures.

B. Verification with simulation

To verify this scheme, we follow the procedure outlined in the last chapter to design a perfect reflector that couples a normal plane incident wave $\theta_i = 0$ to a plane wave reflected with angle $\theta_r = 70^\circ$. In Fig. 7(a) we show the impedance matrix profile within a period $\Lambda = 2\pi/[k(\sin\theta_r - \sin\theta_i)]$. In this case, we set $p_0 = 1$, $|p_{1s}| = 1$, $\phi = \pi/2$, and $k_1 = 3k(\sin\theta_r - \sin\theta_i)$. From the figure, we see that $Z_{12} = Z_{21}$, confirming that the designed field satisfies the local power requirement. The fact that $Z_{11} \neq Z_{22}$ indicates such a metasurface needs bianisotropic unit cells.

The scheme is verified with simulation in COMSOL. The three-membrane approach is adopted to realize the designed impedance matrix profile. The distance between adjacent membranes is set as 5 mm. The calculated impedances for the three membranes are plotted in Fig. 7(b). In realization, the metasurface is discretized into n = 60 unit cells per period. The scattered fields from the theoretical calculation and the simulation are plotted in Figs. 7(c) and 7(d). From the figures, we see excellent agreement between the theoretical calculation and simulation. There is no unwanted scattering, showing the effectiveness of the proposed metasurface design.

IV. SIMULTANEOUS ARBITRARY TRANSMISSION AND REFLECTION CONTROL

In this case, simultaneously arbitrary control of transmission and reflection will be demonstrated with the help of self-excited surface waves. The incident, reflection, and transmitted angles are θ_i , θ_r , and θ_t , and the reflection and transmission coefficients are $R = re^{i\phi_r}$ and $T = te^{i\phi_t}$, respectively. Here T and R follow the global power conservation condition

$$\cos \theta_i - r^2 \cos \theta_r = t^2 \cos \theta_t. \tag{35}$$

Since the intensity variation is determined by the interference between waves, a simple way to design surface waves is to make sure both sides have the same number of wave components, so that the resulting interference contains the same number of components for matching.

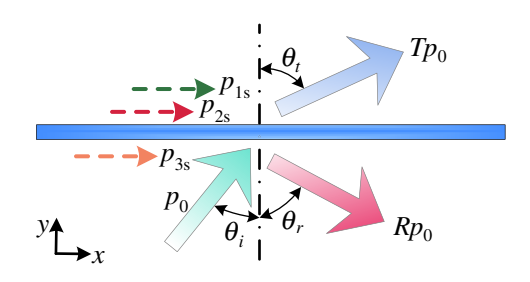


FIG. 8. Illustration of the metasurface for simultaneously arbitrary control of transmission and reflection.

In this case, two surfaces waves on the transmission side and one surface wave on the incident side is assumed, as shown in Fig. 8. The amplitudes of the surface waves are $p_{1s} = a_1 e^{j\beta_1} p_0$, $p_{2s} = a_2 e^{j\beta_2} p_0$, and $p_{3s} = a_3 e^{j\beta_3} p_0$, and their decay rates are α_1 , α_2 , and α_3 . Hence, the wave numbers along the metasurface for these surface waves are $k_1 = \sqrt{k^2 + \alpha_1^2}$, $k_2 = \sqrt{k^2 + \alpha_2^2}$, and $k_3 = \sqrt{k^2 + \alpha_3^2}$, respectively. The pressure field on the incident side is

$$p_{1} = p_{0}e^{-jk\sin\theta_{i}x}e^{-jk\cos\theta_{i}y} + Rp_{0}e^{-jk\sin\theta_{r}x}e^{jk\cos\theta_{r}y} + p_{3s}e^{\alpha_{3}y}e^{-jk_{3}x}.$$
(36)

The pressure and normal velocity fields on the incident side along the metasurface (y = 0) are thus

$$p_{10} = p_0 e^{-jk\sin\theta_i x} + r e^{j\phi_r} p_0 e^{-jk\sin\theta_r x} + p_{3s} e^{-jk_3 x}, \quad (37)$$

$$v_{1,y0} = \frac{p_0 \cos \theta_i}{Z_0} e^{-jk \sin \theta_i x} - r e^{j\phi_r} \frac{p_0 \cos \theta_r}{Z_0} e^{-jk \sin \theta_r x} + \frac{ja_3 \alpha_3 p_0}{kZ_0} e^{-j(k_3 x - \beta_3)}.$$
 (38)

Therefore, the intensity field on the incident side along the metasurface is

$$I_{1,y} = \frac{|p_0|^2}{2Z_0} \cos \theta_i - \frac{|p_0|^2}{2Z_0} r^2 \cos \theta_r$$

$$+ \frac{|p_0|^2}{2Z_0} r(\cos \theta_i - \cos \theta_r)$$

$$\times \cos[k(\sin \theta_i - \sin \theta_r)x + \phi_r]$$

$$+ \frac{|p_0|^2}{2Z_0} a_3 \sqrt{\cos^2 \theta_i + \frac{\alpha_3^2}{k^2}}$$

$$\times \cos[(k_3 - k \sin \theta_i)x - \beta_3 + \gamma_1]$$

$$- \frac{|p_0|^2}{2Z_0} r a_3 \sqrt{\cos^2 \theta_r + \frac{\alpha_3^2}{k^2}}$$

$$\times \cos[(k_3 - k \sin \theta_r)x + \phi_r - \beta_3 + \gamma_2], \quad (39)$$

where $\tan \gamma_1 = -\alpha_3/k \cos \theta_i$ and $\tan \gamma_2 = \alpha_3/k \cos \theta_r$.

On the transmission side, the pressure field is

$$p_{2} = Tp_{0}e^{-jk\sin\theta_{t}x}e^{-jk\cos\theta_{t}y} + p_{1s}e^{-\alpha_{1}y}e^{-jk_{1}x} + p_{2s}e^{-\alpha_{2}y}e^{-jk_{2}x}.$$
(40)

The pressure and normal velocity fields along the metasurface on the transmission side are thus

$$p_{20} = te^{j\phi_t} p_0 e^{-jk\sin\theta_t x} + p_{1s} e^{-jk_1 x} + p_{2s} e^{-jk_2 x}, \tag{41}$$

$$v_{2,y0} = \frac{p_0 \cos \theta_t}{Z_0} t e^{j\phi_t} e^{-jk \sin \theta_t x} - \frac{ja_1 \alpha_1 p_0}{k Z_0} e^{-j(k_1 x - \beta_1)} - \frac{ja_2 \alpha_2 p_0}{k Z_0} e^{-j(k_2 x - \beta_2)}.$$
(42)

Therefore, the intensity field on the transmission side of the metasurface can be calculated as

$$I_{2,y} = \frac{|p_0|^2}{2Z_0} t^2 \cos \theta_t + \frac{|p_0|^2}{2Z_0} t a_1 \sqrt{\cos^2 \theta_t + \frac{\alpha_1^2}{k^2}}$$

$$\times \cos[(k_1 - k \sin \theta_t)x + \phi_t - \beta_1 + \gamma_3]$$

$$+ \frac{|p_0|^2}{2Z_0} t a_2 \sqrt{\cos^2 \theta_t + \frac{\alpha_2^2}{k^2}}$$

$$\times \cos[(k_2 - k \sin \theta_t)x + \phi_t - \beta_2 + \gamma_4]$$

$$+ \frac{|p_0|^2}{2Z_0} \frac{a_1 a_2 (\alpha_2 - \alpha_1)}{k}$$

$$\times \cos\left[(k_1 - k_2)x + \beta_2 - \beta_1 + \frac{\pi}{2}\right], \quad (43)$$

where $\tan \gamma_3 = \alpha_1/k \cos \theta_t$ and $\tan \gamma_4 = \alpha_2/k \cos \theta_t$.

Comparing Eqs. (39) and (43) and using the global power conservation condition in Eq. (35), we find a condition to match the power on both sides by setting

$$k_1 = k_2 + k(\sin \theta_i - \sin \theta_r), \tag{44}$$

$$k_3 = k_2 + k(\sin \theta_i - \sin \theta_t), \tag{45}$$

where k_2 can be arbitrary as long as the resulting k_1 , k_2 , k_3 are all greater than k in magnitude. Once the arbitrary k_2 is chosen, α_1 , α_2 , α_3 , γ_1 , γ_2 , γ_3 , γ_4 are all fixed. The

remaining conditions for matching the power are thus

$$\frac{a_1 a_2 (\alpha_2 - \alpha_1)}{k} = r(\cos \theta_i - \cos \theta_r), \qquad (46a)$$

$$\phi_r = \beta_2 - \beta_1 + \frac{\pi}{2},\tag{46b}$$

$$ta_2\sqrt{\cos^2\theta_t + \frac{\alpha_2^2}{k^2}} = a_3\sqrt{\cos^2\theta_t + \frac{\alpha_3^2}{k^2}},$$
 (46c)

$$-\beta_3 + \gamma_1 = \phi_t - \beta_2 + \gamma_4, \tag{46d}$$

$$ta_1\sqrt{\cos^2\theta_t + \frac{\alpha_1^2}{k^2}} = -ra_3\sqrt{\cos^2\theta_r + \frac{\alpha_3^2}{k^2}},$$
 (46e)

$$\phi_r - \beta_3 + \gamma_2 = \phi_t - \beta_1 + \gamma_3. \tag{46f}$$

Hence, the amplitude and phase of the required surface waves can be solved as

$$a_{1} = -\frac{r}{t} \sqrt{\frac{\cos^{2}\theta_{r} + \alpha_{3}^{2}/k^{2}}{\cos^{2}\theta_{t} + \alpha_{1}^{2}/k^{2}}} a_{3},$$

$$a_{2} = \frac{1}{t} \sqrt{\frac{\cos^{2}\theta_{i} + \alpha_{3}^{2}/k^{2}}{\cos^{2}\theta_{t} + \alpha_{2}^{2}/k^{2}}} a_{3},$$

$$a_{3} = \sqrt{\frac{t^{2}k(\cos\theta_{i} - \cos\theta_{r})}{\alpha_{1} - \alpha_{2}}}$$

$$\times \left[\frac{(\cos^{2}\theta_{t} + \alpha_{1}^{2}/k^{2})(\cos^{2}\theta_{t} + \alpha_{2}^{2}/k^{2})}{(\cos^{2}\theta_{i} + \alpha_{3}^{2}/k^{2})(\cos^{2}\theta_{r} + \alpha_{3}^{2}/k^{2})} \right]^{1/4},$$

$$\beta_{1} = \beta_{3} + \phi_{t} - \phi_{r} + \gamma_{3} - \gamma_{2},$$

$$\beta_{2} = \beta_{3} + \phi_{t} + \gamma_{t} - \gamma_{1}.$$

Here β_3 can be chosen arbitrarily, and we set $\phi_r = \frac{1}{2}(\gamma_1 - \gamma_2 + \gamma_3 - \gamma_4 + \pi/2)$ in order to find a consistent solution. We note that in most applications the reflection phase is not as important as the splitting power and direction. If we need an arbitrary reflection phase as well, k_2 can be carefully selected by solving the above equation to fit this requirement. By simply setting t=0, the problem is reduced to the anomalous reflection case, and from Eqs. (46) we can immediately get the conditions discussed in the previous section.

Once the power profiles on both sides of the metasurface are matched, a purely passive bianisotropic metasurface can be designed, as stated in the previous sections. Here the detailed design is omitted for brevity. We note that if $|\sin \theta_i + \sin \theta_t - \sin \theta_r| > 1$ then one surface wave on the transmission side would be enough to match the intensity profile. The detailed derivation is straightforward and is thus omitted.

V. DISCUSSION AND CONCLUSION

With the addition of evanescent surface waves, we have shown that local power balance on both sides of an acoustic metasurface can be achieved, enabling wavefront conversion with a theoretical power efficiency that can reach 100%. In this paper, we have analyzed the power of such a scheme in both transmission-type and reflection-type metasurfaces. We use two arbitrary beam splitting cases, a perfect reflection case and a simultaneous transmission and reflection control case, to demonstrate the highly efficient wavefront transformation with bianisotropic metasurfaces. For the equal splitting case, the design is verified with both simulation and experiment. In simulations with ten unit cells per period, the power coupled into two desired directions, 51.20% and 48.79%, and the overall power efficiency reaches 99.94%. The experiment showed good agreement with the simulation. The output beams are concentrated in -59° and -58° , with an amplitude ratio of 0.9256. We have also designed a device to split the waves into different directions with a designed intensity ratio. The simulation shows a power efficiency of over 99%. The scheme is also applied to the reflection-type metasurface for the case of anomalous reflection, verified with simulations. In the fourth case, we demonstrate the design of a metasurface that split in an arbitrary way the transmitted and reflected fields at the same time. Note that such an approach is not limited to the control of plane waves. More complex functionalities can be achieved as long as the surface waves are properly designed. Such a feature distinguishes the metasurfaces from other approaches such as metagratings [28–30].

An interesting and counterintuitive finding is that, conventionally, while designing transmission-type metasurfaces we tend to seek unit cells with minimized reflection coefficients, whereas, for reflection-type metasurfaces, hard walls are typically used to eliminate any transmission. However, in this work, we see that, for the metasurface to achieve high power efficiency, we need to allow reflection for the transmission-type metasurfaces and allow controlled transmission for the reflection-type metasurface.

There are a few limitations to this approach. First, it can be easily adapted for simple and periodic wavefront transformations, while for nonperiodic cases, such as focusing or even holograms, the surface waves required to redistribute energy locally can be complicated, and designing them might involve sophisticated optimization tools. Second, in some cases, the wave number for the surface waves

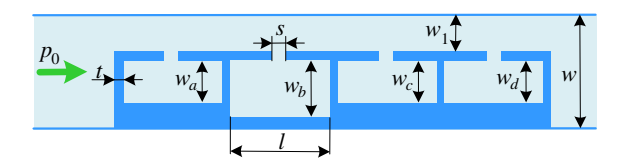


FIG. 9. Schematic view of the four-resonator structure.

can be large, and the required impedance profile fluctuates on very small spatial scales, as we can see in the perfect reflection case. This creates challenges in the experimental realization of such metasurfaces. However, we note that the combinations of surface waves in this paper are chosen to guarantee a reasonable periodicity. In practice, there is nonuniqueness in the selection of the surface waves that can reduce the complexity of the impedance matrix profile. Despite this complexity, we have shown that surface waves dramatically expand the types of wavefront transformations that can be efficiently implemented using acoustic metasurfaces.

ACKNOWLEDGMENTS

This work was supported by a Multidisciplinary University Research Initiative grant from the Office of Naval Research (Grant No. N00014-13-1-0631) and an Emerging Frontiers in Research and Innovation grant from the National Science Foundation (Grant No. 1641084). A.S. wishes to acknowledge the China Scholarship Council (CSC) for financial support (Grant No. 201806280160).

APPENDIX A: GEOMETRIC PARAMETERS FOR THE METASURFACES

The optimized geometric parameters for the metasurfaces described in this paper are discussed in Fig. 9, Tables I and II.

APPENDIX B: PURELY IMAGINARY IMPEDANCE MATRIX FOR RECIPROCAL AND LOSSLESS ACOUSTIC SYSTEMS

For a reciprocal multiport network, the passive and lossless condition will lead to a purely imaginary impedance matrix. Such a condition is well-established for microwaves and multiport circuits [31]. Following the results for the multiport circuits, an acoustic version can be derived. Consider a reciprocal lossless N-port acoustic device. If the device is lossless, the net real power delivered to the device must be zero for any boundary condition applied at each port. Thus, Re[I] = 0, where

$$I = \frac{1}{2}[p]^{T}[v]^{*}$$

$$= \frac{1}{2}([Z][v])^{T}[v]^{*}$$

$$= \frac{1}{2}[v]^{T}[Z][v]^{*}$$

$$= \frac{1}{2}(v_{1}Z_{11}v_{1}^{*} + v_{1}Z_{12}v_{2}^{*} + v_{2}Z_{21}v_{1}^{*} + \cdots)$$

$$= \frac{1}{2}\sum_{n=1}^{N}\sum_{m=1}^{N}v_{m}Z_{mn}v_{n}^{*}.$$
(B1)

If we apply hard boundary at every port except for the *n*th port, we immediately have

$$Re[v_n Z_{nn} v_n^*] = |v_n|^2 Re[Z_{nn}] = 0.$$
 (B2)

Therefore, the diagonal terms in the impedance matrix Z_{nn} shall be purely imaginary. Now apply a hard boundary to all ports except for the *m*th and *n*th ports. Since $Z_{nm} = Z_{mn}$ for reciprocal devices, we obtain

$$Re[(v_n v_m^* + v_m v_n^*) Z_{mn}] = 0.$$
 (B3)

Because $(v_n v_m^* + v_m v_n^*)$ is purely real and, in general, nonzero, we must have $Re[Z_{mn}] = 0$ for any m and n. Hence, any reciprocal and lossless N-port acoustic system will have a purely imaginary impedance matrix.

TABLE I. Design parameters of the individual resonators of the scattering-free bianisotropic metasurface to split a normally incident wave into $\pm 60^{\circ}$ waves, implemented with ten cells within one period.

Cell	Cost	w	w_1	w_a	w_b	w_c	w_d
1	0.10	13.2	3.24	5.77	5.68	7.51	1.65
2	0.04	13.2	4.31	6.77	5.84	6.63	3.68
3	2.39	13.2	1.33	6.29	9.18	7.77	5.61
4	1.81	13.2	1.62	5.33	0.01	9.38	5.63
5	0.07	13.2	1.81	7.04	7.58	6.39	6.63
6	56.79	13.2	1.38	4.24	7.82	5.48	9.74
7	0.18	13.2	1.37	5.12	4.73	5.86	7.22
8	1.23	13.2	1.71	5.52	0.01	9.47	5.79
9	0.74	13.2	1.24	6.00	9.04	7.48	5.39
10	0.05	13.2	4.10	6.35	4.93	6.54	4.71

TABLE II. Design parameters of the individual resonators of the scattering-free bianisotropic metasurface to split a normally incident wave into two waves with transmitted angles $\theta_1 = 36.87^{\circ}$, $\theta_2 = 64.16^{\circ}$ and transmission coefficients $t_1 = 0.99$, $t_2 = 0.70$, implemented with 30 cells within one period.

Cell	Cost	w	w_1	w_a	w_b	w_c	w_d
1	0.02	12.7	3.67	4.61	0.32	3.09	6.75
2	0.02	12.7	4.94	4.80	2.04	3.54	5.36
3	0.15	12.7	1.49	6.58	8.42	5.89	7.87
4	85.68	12.7	1.57	5.34	0	9.13	6.74
5	0.16	12.7	1.35	6.96	6.31	0	4.68
6	0.08	12.7	1.84	6.43	6.87	6.74	7.77
7	0.09	12.7	1.49	6.46	7.62	4.90	5.05
8	1.10	12.7	1.59	7.29	6.09	2.98	6.30
9	0.19	12.7	1.89	4.59	4.05	8.63	6.05
10	0.95	12.7	1.40	6.63	9.30	7.97	7.16
11	0.02	12.7	2.87	4.88	3.72	1.46	7.15
12	14.62	12.7	2.79	5.16	7.20	6.73	2.37
13	6.76	12.7	2.62	7.35	6.88	3.94	1.97
14	0.09	12.7	2.87	6.91	3.40	4.62	3.71
15	10.63	12.7	3.35	6.98	0.01	0	6.01
16	0.05	12.7	1.05	5.53	7.45	4.01	4.68
17	0.05	12.7	1.46	7.75	6.74	6.87	5.07
18	127.02	12.7	5.77	3.91	0.10	0.51	2.27
19	119.2	12.7	6.22	4.34	0	0	2.68
20	352.22	12.7	9.70	0.14	1.01	0	0
21	0.29	12.7	1.71	6.13	0	7.19	8.13
22	27.36	12.7	1.63	5.28	0	9.08	5.99
23	0.73	12.7	1.79	3.61	4.13	8.14	5.52
24	0.17	12.7	1.99	6.99	8.23	3.34	4.59
25	5.95	12.7	2.23	5.64	0	7.48	8.31
26	0.32	12.7	1.42	5.38	6.90	3.43	2.58
27	0.02	12.7	2.02	5.26	0.53	1.05	7.76
28	215.09	12.7	3.14	7.52	0.05	0.01	6.12
29	3.02	12.7	3.58	6.75	0	0.06	3.87
30	0.01	12.7	3.78	4.94	1.18	2.60	6.08

- [1] N. I. Zheludevand and Y. S. Kivshar, From metamaterials to metadevices, Nat. Mater. 11, 917 (2012).
- [2] S. A. Cummer, J. Christensen, and A. Alù, Controlling sound with acoustic metamaterials, Nat. Rev. Mater. 1, 16001 (2016).
- [3] G. Maand and P. Sheng, Acoustic metamaterials: From local resonances to broad horizons, Sci. Adv. 2, e1501595 (2016).
- [4] Y. Li, X. Jiang, R.-Q. Li, B. Liang, X.-Y. Zou, L.-I. Yin, and J.-C. Cheng, Experimental Realization of Full Control of Reflected Waves with Subwavelength Acoustic Metasurfaces, Phys. Rev. Appl. 2, 064002 (2014).
- [5] Y. Xie, W. Wang, H. Chen, A. Konneker, B.-I. Popa, and S. A. Cummer, Wavefront modulation and subwavelength diffractive acoustics with an acoustic metasurface, Nat. Commun. 5, 1 (2014).
- [6] Y. Xie, A. Konneker, B.-I. Popa, and S. A. Cummer, Tapered labyrinthine acoustic metamaterials for broadband impedance matching, Appl. Phys. Lett. 103, 201906 (2013).
- [7] Y. Xie, B.-I. Popa, L. Zigoneanu, and S. A. Cummer, Measurement of a Broadband Negative Index with

- Space-Coiling Acoustic Metamaterials, Phys. Rev. Lett. 110, 175501 (2013).
- [8] Y. Li, X. Jiang, B. Liang, J.-C. Cheng, and L. Zhang, Metascreen-Based Acoustic Passive Phased Array, Phys. Rev. Appl. 4, 024003 (2015).
- [9] X. Zhu, K. Li, P. Zhang, J. Zhu, J. Zhang, C. Tian, and S. Liu, Implementation of dispersion-free slow acoustic wave propagation and phase engineering with helical-structured metamaterials, Nat. Commun. 7, 1 (2016).
- [10] Y. Tian, Q. Wei, Y. Cheng, and X. Liu, Acoustic holography based on composite metasurface with decoupled modulation of phase and amplitude, Appl. Phys. Lett. **110**, 191901 (2017).
- [11] Z. Jia, J. Li, C. Shen, Y. Xie, and S. A. Cummer, Systematic design of broadband path-coiling acoustic metamaterials, J. Appl. Phys. 123, 025101 (2018).
- [12] J. P. Wong, A. Epstein, and G. V. Eleftheriades, Reflectionless wide-angle refracting metasurfaces, IEEE Antennas Wirel. Propag. Lett. **15**, 1293 (2015).
- [13] N. M. Estakhriand and A. Alù, Wave-Front Transformation with Gradient Metasurfaces, Phys. Rev. X 6, 041008 (2016).
- [14] V. S. Asadchy, M. Albooyeh, S. N. Tcvetkova, A. Díaz-Rubio, Y. Ra'di, and S. Tretyakov, Perfect control of

- reflection and refraction using spatially dispersive metasurfaces, Phys. Rev. B **94**, 075142 (2016).
- [15] A. Díaz-Rubio, V. S. Asadchy, A. Elsakka, and S. A. Tretyakov, From the generalized reflection law to the realization of perfect anomalous reflectors, Sci. Adv. 3, e1602714 (2017).
- [16] A. Díaz-Rubioand and S. A. Tretyakov, Acoustic metasurfaces for scattering-free anomalous reflection and refraction, Phys. Rev. B 96, 125409 (2017).
- [17] J. Li, C. Shen, A. Díaz-Rubio, S. A. Tretyakov, and S. A. Cummer, Systematic design and experimental demonstration of bianisotropic metasurfaces for scattering-free manipulation of acoustic wavefronts, Nat. Commun. 9, 1 (2018).
- [18] A. Epsteinand and G. V. Eleftheriades, Synthesis of Passive Lossless Metasurfaces Using Auxiliary Fields for Reflectionless Beam Splitting and Perfect Reflection, Phys. Rev. Lett. 117, 256103 (2016).
- [19] L. Quanand and A. Alù, Passive Acoustic Metasurface with Unitary Reflection Based on Nonlocality, Phys. Rev. Appl. 11, 054077 (2019).
- [20] A. Díaz-Rubio, J. Li, C. Shen, S. A. Cummer, and S. A. Tretyakov, Power flow—conformal metamirrors for engineering wave reflections, Sci. Adv. 5, eaau7288 (2019).
- [21] V. S. Asadchy, A. Díaz-Rubio, and S. A. Tretyakov, Bianisotropic metasurfaces: Physics and applications, Nanophotonics 7, 1069 (2018).
- [22] M. B. Muhlestein, C. F. Sieck, P. S. Wilson, and M. R. Haberman, Experimental evidence of willis coupling in a one-dimensional effective material element, Nat. Commun. 8, 1 (2017).

- [23] L. Quan, Y. Ra'di, D. L. Sounas, and A. Alù, Maximum Willis Coupling in Acoustic Scatterers, Phys. Rev. Lett. 120, 254301 (2018).
- [24] A. Melnikov, Y. K. Chiang, L. Quan, S. Oberst, A. Alù, S. Marburg, and D. Powell, Acoustic meta-atom with experimentally verified maximum willis coupling, Nat. Commun. 10, 1 (2019).
- [25] J. Li, A. Díaz-Rubio, C. Shen, Z. Jia, S. Tretyakov, and S. Cummer, Highly Efficient Generation of Angular Momentum with Cylindrical Bianisotropic Metasurfaces, Phys. Rev. Appl. 11, 024016 (2019).
- [26] A. Epsteinand and G. V. Eleftheriades, Arbitrary power-conserving field transformations with passive lossless omega-type bianisotropic metasurfaces, IEEE Trans. Antennas Propag. 64, 3880 (2016).
- [27] Z. Hou, X. Fang, Y. Li, and B. Assouar, Highly Efficient Acoustic Metagrating with Strongly Coupled Surface Grooves, Phys. Rev. Appl. 12, 034021 (2019).
- [28] D. Torrent, Acoustic anomalous reflectors based on diffraction grating engineering, Phys. Rev. B 98, 060101 (2018).
- [29] P. Packo, A. N. Norris, and D. Torrent, Inverse Grating Problem: Efficient Design of Anomalous Flexural Wave Reflectors and Refractors, Phys. Rev. Appl. 11, 014023 (2019).
- [30] H. Ni, X. Fang, Z. Hou, Y. Li, and B. Assouar, Highefficiency anomalous splitter by acoustic meta-grating, Phys. Rev. B **100**, 104104 (2019).
- [31] D. M. Pozar, *Microwave Engineering* (John Wiley & Sons, Amherst, MA, USA, 2009).